# Toward GaSb-Based Monolithically Integrated Widely-Tunable Lasers for Extended Short- and Mid-Wave Infrared Wavelengths

Weicheng You, Sarvagya Dwivedi, *Member, IEEE*, Imad I. Faruque, Demis D. John,
Anthony P. McFadden, Christopher J. Palmstrøm, *Fellow, IEEE*, Larry A. Coldren, *Life Fellow, IEEE*,
and Shamsul Arafin, *Senior Member, IEEE*

*Abstract*— A fully-functional photonic integrated circuit (PIC) platform with supporting active and passive components in the extended short- and mid-wave infrared spectral regime is of significant research interest for next-generation optical systems. Here we design offset quantum well-based photonic integrated circuits which primarily consist of four section-based widely tunable single-mode lasers emitting at 2560 nm. The platform requires the selective removal of InGaAsSb multi-quantum wells located above a GaSb-based optical waveguide layer and then subsequent single blanket GaSb regrowth. Encouraging preliminary experimental results on regrowth are also reported to confirm the feasibility of the proposed PICs. The simulation result for the tunable laser design shows that a tuning range as wide as ∼120 nm is possible. The quasi-theoretical work performed here is an initial step towards demonstrating complex non-telecommunication PICs which could offer a comprehensive range of photonic functionalities.

*Index Terms*— Photonic integrated circuit, GaSb, S-MWIR, phase tuner, sampled-grating.

## I. INTRODUCTION

**R**ECENTLY, extended short- and mid-wave infrared (S-MWIR) spectral regimes have gained considerable attention to enable a whole range of emerging applica-

tions including biochemical sensing [1], [2], quantum sensing [3], industrial process control [4], and non-invasive medical diagnostics [5], [6]. The S-MWIR wavelength regime is important because it contains a number of spectral features such as strong overtones and a combination of molecular absorption bands in gas- and liquid-phase molecules for sensing applications [7], [8]. S-MWIR devices operating especially at the molecular fingerprint region, $2 \ \mu m < \lambda < 6 \ \mu m$ result in unprecedented sensitivity and selectivity when it comes to photonic sensors [9], [10]. This eye-safe spectral regime also has an atmospheric transmission window, which makes it suitable for light detection and ranging (LiDAR) or free-space communication applications [11].

Considering all these real-world applications, several discrete active [12] and passive [13], [14] photonic devices operating at the S-MWIR wavelength regime have been developed for years. However, little progress has been made in the development of PIC-compatible S-MWIR active devices, including broadband and continuously tunable lasers, and semiconductor optical amplifiers (SOAs), as well as their on-chip monolithic integration with passive devices. Highly-integrated S-MWIR PICs will not only provide low-size, -weight, -power and -cost (SWaP-C) advantages but also bring transformative changes to on-chip sensing applications.

For spectroscopy, conventional type-I diode lasers emitting at 2.2-3.4 $\mu m$ [15], [16], [17] and interband cascade lasers (ICLs) at 3-6 $\mu m$ [12], [18], [19], [20], [21] offer compelling SWaP-C reduction advantages over quantum cascade lasers (QCLs) that are a more mature technology for wavelengths $\lambda \geq 4.5 \ \mu m$ [22], [23]. In particular, type-I or ICLs in the S-MWIR regime consume nearly an order of magnitude less power than the power-hungry QCLs [24]. This is highly advantageous in handheld, battery-operated and even solar-powered photonic subsystems based on type-I lasers or ICLs. While QCLs can produce higher maximum output powers, this does not pose a problem for photonic sensors or spectrometers because typical type-I or ICL outputs on the order of mW are adequate for most absorption spectroscopy applications. Importantly, one key component of a PIC is an SOA, suggesting that the power output of a single laser is not necessarily the maximum output of the PIC.

From the material perspective, even though gallium antimonide (GaSb) and its alloys are relatively less mature, they comprise the optimal material system for integrating 2.2-6 $\mu$m lasers on PICs. This contrasts with standard and mature material platforms such as InP, which experience a significant performance droop for gain chips at wavelengths $\geq$1.7 $\mu$m. Although there are a few reports on InP-based lasers emitting up to 2.4 $\mu$m [25], [26], highly-strained type-I quantum wells as a gain medium were utilized in these studies. Hence, InP and its alloys are less attractive due to such material limitations for making high-performance PICs at the specified wavelength regime.

Widely-tunable lasers based on surface gratings are one of the basic and critical active components in realizing fully-functional PICs. Despite significant technological achievements in monolithic InP PICs with sampled-grating distributed Bragg reflector (SG-DBR)- [27] and ring resonator- [28] lasers at 1.55 $\mu$m over the past few decades, such a platform in the S-MWIR regime has not yet reached its full potential. A framework and clear roadmap for developing monolithic GaSb PICs using an ICL material system for the wavelength range of 3-6 $\mu$m has recently been reported [29]. Among basic optical passive components at S-MWIR, low-loss optical waveguides [13], [30], fiber-to-chip grating couplers [13], ring resonators [31], wavelength demultiplexers based on arrayed waveguide grating [14], [32] were developed using silicon-on-insulator (SOI) wafers that are transparent up to a wavelength of 4 $\mu$m [33]. There are also few demonstrations on heterogeneously integrated InP gain materials on silicon PICs reported around 2.3 $\mu$m wavelengths [34], [35], [36]. Recently, PICs have been demonstrated using heterogeneous integration of GaSb-active devices with SOI passive components. In particular, S-MWIR ICLs using GaSb were integrated on SOI through heterogeneous integration [37], [38], [39], [40]. Hybrid integration is another promising route, and GaSb/SOI hybrid tunable lasers with emission wavelengths up to 2.7 $\mu$m were reported [41]. Though a monolithic platform offers more flexibility and compactness, heterogenous- and hybrid- integration platforms provide several advantages, including low-loss waveguides, high-performance passives, high-coupling efficiency, and low-cost wafer-scale assembly.

By employing an InGaAsSb/AlGaAsSb/GaSb material and necessary processing steps, as well as by leveraging the technological advancement in the GaSb material system, developing S-MWIR PICs technology is possible. This paper will primarily discuss about the design of GaSb-based widely-tunable lasers by monolithically integrating functional components on the same substrate in order to have the greatest impact. SG-DBR lasers are four-section devices with four separate electrodes for controlling a gain section, a phase tuner and two mirrors which are connected by waveguides – yielding a small version of complete PICs. This will pave the way for implementing complex PICs which will simultaneously improve performance and efficiency as well as help meet low SWaP-C constraints for next-generation S-MWIR photonic technologies.
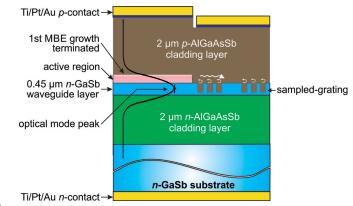


Fig. 1. Schematic cross-sectional view of an offset quantum-well SG-DBR laser cavity with an emission wavelength of 2.6 $\mu$m. The transverse-mode intensity profile is also schematically shown in the laser structure (not drawn to scale).

## II. ACTIVE-PASSIVE INTEGRATION PLATFORM

Processing on the native III-V chip rather than silicon is generally more straightforward and less expensive, and likely to produce a higher yield. Several commonly used active-passive integration platforms include offset quantum well (OQW) [42], [43] and quantum well intermixing (QWI) [44] in monolithic designs, and vertical taper coupling in heterogenous designs [45]. In this study, the monolithic OQW integration platform was considered, which requires a relatively simple process. A schematic cross-sectional view of the active/passive interface within the GaSb-based SG-DBR laser is illustrated in Fig. 1. The SG-DBR lasers provide a tunable component limited to ~6% of the center wavelength in order to obtain a good side-mode suppression ratio using a simple cavity geometry. SG-DBR lasers are four-section devices with four separate electrodes for controlling gain section, phase modulator and two mirrors which are connected by waveguides – yielding a small version of complex PICs. Electrical isolation between the sections of the PICs can be achieved either by spatially-defined etched trenches or high-resistance ion implanted regions. Ion implantation on antimonides has recently been pursued and promising preliminary results were achieved [46], [47]. Key challenges for the successful demonstration of S-MWIR PICs include sufficient cleaning of the sample surface after patterning of the base structure, the subsequent regrowth of defect-free top cladding layers, lack of selective wet and dry etching processes, immature PIC-enabling technologies, and the fast oxidation of GaSb.

## III. WAVEGUIDE STRUCTURES

A lateral waveguide architecture usually has a great impact on the design of PICs. There are four most commonly used waveguide structures including buried rib, surface ridge, buried channel, and deeply-etched ridge waveguides. All of these can be formed with a single blanket regrowth of semiconductor cladding, which does not involve any foreign masking material on the wafer surface to define epitaxial

regrowth dynamics. Among these, the surface ridge waveguide has a good current confinement, and lower loss for single-mode waveguides, which makes it uniquely suitable for lasers [48]. Hence, the surface ridge waveguide was used in the design.

## IV. WIDELY TUNABLE LASERS

### A. Device Structure

A base structure, containing the lower cladding, the optical waveguide and the multiple-quantum-well (MQW) layers, is required to be grown first. This allows for the selective etching removal of the MQW in regions where gain is not required, leaving a non-absorbing waveguide. Then, after removing the MQWs from regions where passive waveguides are desired, a second 'regrowth' is essential to apply the top cladding and the top contact in all regions. An unpatterned cladding regrowth is often performed with only a small or negligible height change between the active and passive regions [49]. For SG-DBR lasers at this long emission wavelength, the right top and bottom cladding materials with the right thickness and correct bandgap are used so that the optical mode decays fast and the highly-doped, narrower-bandgap top $p$-contact layer and the bottom substrate do not see the fundamental transverse mode.

In the OQW platform, the MQW active region is deliberately placed on top of the waveguide. In this configuration, the optical mode overlap with the QWs is not as high as possible and by definition, the same is true of the modal gain. However, as mentioned above, this greatly facilitates the active/passive fabrication process. The goal is to maintain sufficient optical mode overlap with QWs while reducing the overlap with the substrate and highly doped contact layer. To characterize our active and passive sections, a two-dimensional finite difference Eigenmode solver from Ansys Lumerical MODE [50] was used to perform simulations on a cross section of the waveguides. Ansys' built-in confinement calculator was used to compute the optical confinement factors of each layer of the waveguides as listed in Table I.

Fig. 2 (top) shows the 1D and 2D intensity distribution of the fundamental transverse mode in 2.6 $\mu$m OQW SG-DBR laser structures. Despite a lower refractive index of the waveguide layer compared to the QWs, the mode overlap with the 450-nm-thick waveguide layer is substantial. This is because of the thin QWs (total 70 nm) in the active region that only add a small perturbation to the optical mode. The intensity distribution together with the refractive index profile is also shown. The optical confinement factor $\Gamma$ of a semiconductor laser is of utmost importance. An increase in the confinement factor of the active QWs yields an increase in the modal gain. For low-loss optical waveguides, it is also important to simulate the transverse mode for the passive region with the MQW region removed. Fig. 2 (bottom) shows the 1D and 2D intensity distribution of the fundamental transverse mode in the passive region of the 2.6 $\mu$m laser structures. The intensity distribution together with the refractive index profile is also shown here. Table I lists the $\Gamma$ values for several sections in the active and passive regions.



Fig. 2. Cross section of a 2.6 $\mu$m OQW SG-DBR laser structure in the active (top) and passive (bottom) regions along with 2D surface plot of the light intensity of the fundamental transverse mode, where the waveguide effective refractive index $n_{\text{eff}} = 3.61$, 1D intensity distribution of the fundamental TE-mode in the waveguide, and refractive index profile and mode intensity distribution.

### B. Growth Technology

The two most popular methods available for epitaxial growth of the GaSb-based laser structures are molecular beam epitaxy (MBE) and metalorganic chemical vapor deposition (MOCVD). Although MOCVD is generally preferred for commercialization purposes, progress made to antimonide-growth has been greatly hindered due to technical challenges such as non-ideal growth conditions imposed by competing needs of typical III-Sb processes (i.e. low growth temperature) and typical precursors (i.e. inefficient pyrolysis at low temperatures). Therefore, MBE is still considered to be the preferred technology for the growth of GaSb and its alloys. GaSb as grown by MBE is known to be natively $p$-type due to the high number of GaSb antisite defects. In the active part, the GaSb waveguide layer has to be weakly $n$-doped so that it

TABLE I
CONFINEMENT FACTORS IN ACTIVE AND PASSIVE SECTIONS OF THE
WAVEGUIDE

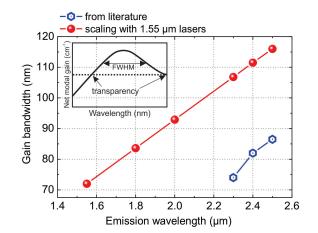| Optical mode in | Confinement factors (active) | Confinement factors (passive) |
|---|---|---|
| 7 QWs | 7.6% | N/A |
| Top & bottom cladding | 15% + 14.3% | 19.8% + 22% |
| Waveguide | 53.8% | 55.3% |
| $n$-substrate | 0.01% | 0.01% |
| $n^+$ contact layer | $10^{-4}$% | $4 \times 10^{-4}$% |



Fig. 3. Spectral gain bandwidth as a function of wavelength, where theoretical gain bandwidth values based on simple-scaling from 1.55 $\mu$m (red circles), and experimentally measured values (blue hexagons) were collected from the literature.

can conduct electrons to the MQW region. In the passive part, depletion regions of a *p-n* junction should be roughly in the middle of the structure. Placement of the *p-n* junction within the structure is important because it ensures good carrier injection into this lower bandgap waveguide region for good tuning. Considering this, it is important to weakly dope about half of the GaSb layer to be *n*-type in order to actually compensate the intrinsic disorders of GaSb.

### C. Tuning Range

The spectral gain bandwidth of S-MWIR lasers in the literature as well as extrapolations of the tuning ranges of SG-DBR lasers at 1.55 $\mu$m were undertaken. From the literature, tuning range values of such lasers were estimated from the experimentally measured amplified spontaneous emission spectra of the processed Fabry Pérot lasers [51], [52], [53]. In fact, the net modal gain spectra of the device active regions for the wavelength range of 2.2-2.5 $\mu$m were measured as a function of the excitation current in these experimental studies. Although these measured GaInAsSb gain curves are more realistic, they perhaps yield conservative estimates. In this study, the tuning range of SG-DBR lasers $\Delta\lambda$ was estimated from the full width at half maximum (FWHM) of the gain material. Figure 3 shows the gain bandwidth values obtained from the literature as a function of emission wavelengths. We also considered the relative bandwidth $\Delta\lambda/\lambda$ with respect to the central wavelength that provides a convenient measure of the tuning range. Given the dependence on the central wavelength, the laser's tuning range scales with the center wavelength that the device emits at. Simple scaling of the best result from InP-based SG-DBR at 1.55 $\mu$m is probably optimistic, because optimized devices with tuning ranges as high as 72 nm were reported [27]. Considering this simple scaling, we estimated a highest tuning range scaled to the 2.56 $\mu$m spectral regime.

$$\Delta\lambda_{@2.56\mu m} = 72 \text{ nm} \times \frac{2.56 \ \mu m}{1.55 \ \mu m} \qquad (1)$$

Hence, the tuning range is conservatively estimated to be 120 nm. The linear scaling is valid for the SG-DBR if the waveguide dispersion is similar. That is, the frequency response of the SG-DBR is linearly related to the Fourier transform of the spatial grating pattern and this scales inversely with grating bursts. Considering the group refractive index of the antimonide waveguide, the laser tuning range defined by FWHM envelope bandwidth ($\lambda_{env}$) of mirrors was also

calculated, which is in agreement with the value calculated by the linear scaling.

$$\Delta\lambda_{env} = \frac{\lambda^2}{2n_g Z_1} = 119 \text{ nm @ 2.56 } \mu m$$

where $Z_1$ is the grating burst length, and $n_g$ group index. In addition, a large tuning range in such devices requires a sufficient spectral gain bandwidth from the active region.

### D. Waveguide Design

*1) Thickness:* The thickness of the transverse waveguide layer plays an important role on the device performance in OQW SG-DBR lasers. Thanks to the 2.56 $\mu$m design, this uses binary GaSb material as a waveguide layer. The goal is to maximize the optical mode overlap with the QWs and minimize the overlap with the substrate and contacts by optimizing the thickness and by choosing the right material. In the OQW-based design, there is a trade-off between the QW overlap and the tuning efficiency in the waveguide layer. Using a thicker waveguide layer will increase the amount of index tuning that can be achieved. However, this will reduce the QW overlap and lower the available modal gain as can be seen in the left portion of Fig. 4(a). Increasing the number of QWs to compensate for the reduced overlap will increase the threshold current as well as the coupling loss between the active and passive sections due to the mode mismatch.

For the passive section, the dependence of the mode overlap with the waveguide and the doped substrate on the waveguide thickness is shown in the right portion of Fig. 4(b). As can be seen, with a 450-nm-thick waveguide layer, our design provides good optical mode overlap in the active and passive regions. Therefore, a thickness of 450 nm is chosen in this study. It should be noted that the overlap of the transverse mode with the thickness of 450-nm for the waveguide is calculated to be 55.3%. At this point, one can introduce the transverse confinement factor $\Gamma_{y,\text{waveguide}}$ for the waveguide,

**(a)**



**(b)**


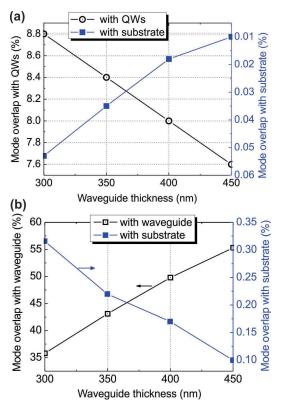
Fig. 4. Optical mode overlap as a function of waveguide thickness for offset quantum well. (a) Active region, and (b) passive region—MQW removed.

TABLE II
DESIGN PARAMETERS FOR ~2.6 $\mu$M SG-DBR MIRROR

| Mirror Characteristics | Value | Unit |
|---|---|---|
| Group index (passive) | 3.93 | |
| Center wavelength | 2560 | nm |
| Etch depth | 85 | nm |
| Grating coupling coefficient $\kappa$ | 300 | cm$^{-1}$ |
| Front Mirror | $N_{FM} = 5$<br>$Z_1 = 7$<br>$Z_0 = 80$ | <br>$\mu$m<br>$\mu$m |
| Back mirror | $N_{BM} = 12$<br>$Z_1 = 7$<br>$Z_0 = 90$ | <br>$\mu$m<br>$\mu$m |
| $L_{eff,BM}$<br>$L_{eff,FM}$ | 196<br>122 | $\mu$m<br>$\mu$m |
| Tuning range based on RMS | 84.5 | nm |
| Envelope bandwidth | 119 | nm |
| $\Delta\lambda_{FWHM, BM}$ | 2.1 | nm |
| $\Delta\lambda_{m,cavity}$ | 0.75 | nm |
| # of cavity modes within $\Delta\lambda_{FWHM, BM}$ | 3 | |

which can be written as [54].

$$\Gamma_{y,\text{waveguide}} = \frac{V_t^2}{2 + V_t^2} \qquad (2)$$

where $V_t$ is a dimensionless normalized frequency parameter for the transverse direction. Using the fundamental single-mode condition for $V = 3.14$, $\Gamma_{y,\text{waveguide}} = 83\%$. Hence, this thickness results in a single-mode waveguide and provides a safety margin from appearing the next higher order mode. However, we need to make sure $\Gamma_{y,\text{QWs}}$ does not get too small.

*2) Width:* Knowing the waveguide and cladding refractive indices, it is possible to apply single fundamental mode condition to find the maximum width of the waveguide. Again, lateral normalized frequency parameter $V_l$ can be represented by the following relation [54].

$$V_l = \frac{2\pi}{\lambda} w \sqrt{n_{\text{eff,wg}}^2 - n_{\text{eff,cl}}^2} \qquad (3)$$

where $\lambda$ is the lasing wavelength, $w$ the waveguide width, $n_{\text{eff,wg}}$ and $n_{\text{eff,cl}}$ the effective refractive indices of the surface ridge waveguide and the -etched region, respectively. Using the single-mode condition $V_l < \pi$, $n_{\text{eff,wg}} = 3.57$, $n_{\text{eff,cl}} = 3.5$ and assuming no optical loss, the maximum width of a surface ridge waveguide can be calculated to be ~1.9 $\mu$m. That means, SG-DBR lasers at 2.56 $\mu$m with $w \geq 1.9$ $\mu$m are supposed to support multiple transverse modes. But experimentally, devices with larger widths (compared to the values estimated here) are observed to emit a single fundamental mode [55]. Especially, one usually ignores the first higher-order odd mode in a laser cavity because it receives very low gain due to a null

in the center of the waveguide. Instead, one really focuses on the first higher-order even mode as the one that receives gain. Hence, the modified single-mode condition in lasers is $V = 2\pi$, yielding the maximum allowable width to be ~3.8 $\mu$m at 2.56 $\mu$m. Moreover, single-mode lasers may have a lateral waveguide width that supports multiple modes but only the fundamental mode lases. The reason behind this is mode-selective loss and gain in the cavity. In other words, the net losses for the higher order modes are higher, and the net gain for the fundamental mode is higher, and thus single lateral mode operation is preferred.

In summary, for a surface-ridge waveguide, single-mode operation can be expected with a ~4-5 $\mu$m waveguide width, but for a deep-ridge waveguide, due to the high confinement, the ridge should be somewhat narrower, < 3 $\mu$m, at this wavelength.

*E. Mirror Design*

The design of the sampled-grating mirrors is critical for the SG-DBR laser operation. To this end, the design criteria of the SG-DBR mirrors that employs the Vernier effect between front and back mirrors to achieve wide tuning will be reviewed. To determine the mirror characteristics, it is very important to have the dispersion data of grating mirror materials. For 2.6 $\mu$m SG-DBR lasers, the sampled-grating mirror consists of a corrugation between the $n$-GaSb waveguide and the $p$-AlGaAsSb cladding. In addition, having knowledge of the group refractive index of the waveguide material, i.e. GaSb in this case is also very important in order to determine the physical parameters involved in SG-DBR mirror design. The wavelength-dependent refractive indices of the mirror materials as well as the group refractive index of GaSb are also used for the design. There are physical parameters, listed in Table II, that determine the reflectivity spectrum of the SG-DBR mirror. The comb-like spectrum is shown in Fig. 5.

The physical parameters are the length of the sampling period $Z_0$, the burst length $Z_1$, the number of periods $N$,
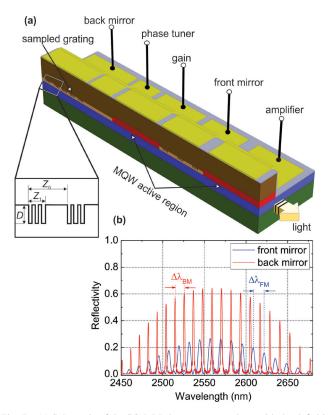
Fig. 5. (a) Schematic of the SG-DBR laser structure along with the definition of the sampled grating mirror. To boost the optical power and for PIC testing, monolithically integrated SOAs after the tunable laser are also shown, and (b) calculated front and back SG-DBR mirror spectra.



Fig. 6. Schematic band diagram of the active region used in broad-area FP laser and then SG-DBR lasers.

TABLE III
DETAILS OF THE ACTIVE REGION

| | |
|---|---|
| Cladding | $Al_{0.5}GaAs_{0.04}Sb$ |
| Barrier | GaSb |
| QWs | $Ga_{0.57}In_{0.43}As_{0.15}Sb_{0.85}$ |
| Barrier thickness | 8 nm |
| QWs thickness | 10 nm |
| Compressive strain - QW (relaxed) | 1.5% |
| QW bandgap (calculated) | 446 meV |
| Quantization energies ($E_C+E_V$) | 23 + 5 meV |
| Emission wavelength (calculated) | 2616 nm |
| Band offset conduction band | 212 meV |
| Band offset valence band | 48 eV |

grating-coupling coefficient $\kappa$ and the grating etch depth $D$. Table II lists parameters of an example design for an SG-DBR laser at 2.6 $\mu$m. It uses numerical values of the gain material taken from [56]. Various other parameters were iterated until a reasonable design was achieved. However, further design effort will be necessary before a final design is complete.

*F. Active Region Design*

In an SG-DBR or other DBR structures, it is desired to first only grow up through MQW layers, remove these regions where passive waveguides, gratings, or other passive components are desired, and then finally complete the PIC by re-growing top cladding over all regions. To successfully accomplish all these GaSb-PIC technology development-related tasks, we chose a wavelength of around 2.6 $\mu$m. Reasons of choosing this wavelength include knowledge availability of experimentally-proven InGaAsSb-based type-I multi-quantum well active regions, less technical difficulty of growing an active region, ease of getting a good QW/barrier interface and subsequent blanket MBE regrowth on Al-free surfaces. All these can be ensured by the well-studied InGaAsSb/GaSb active region-based lasers emitting around 2.6 $\mu$m with a record-low threshold current density at infinite lengths [56], [57], [58].

Some of the key data from the prior published work of S. Arafin on a similar quantum well gain region [56] are utilized here to obtain numerical values for the projected threshold ga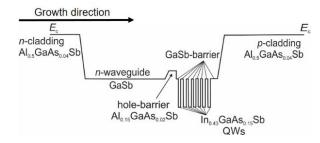in and current levels. As shown in Fig. 6, the active region consists of seven QWs embedded in a GaSb separate confinement waveguide. The QWs are compressively strained and 10 nm thick and they are interfaced with lattice-matched 8 nm thick binary GaSb barriers. The outer parts of the QWs are also surrounded by undoped GaSb barriers. A 30-nm-thick $n$-doped $Al_{0.15}GaAs_{0.02}Sb$ layer is included as a hole barrier on the $n$-side to prevent hole leakage from the valence band of the QWs. Details of the active region are listed in Table III. Since there is not so much valence band offset, it is important to make the layer doped deliberately to keep most of the band offset in the valence band. Diagnostic laser structures were grown, and broad-area lasers were fabricated to de-embed numerous important material and device parameters. The test broad-area lasers exhibited near state-of-the art threshold-current densities, as well as injection efficiencies, waveguide losses, and gain parameters, in-line with some of the reported numbers [56], [57], [58].

Gain constant ($g_o$) for the active region material and transparency current density $J_{tr}$ are two important laser parameters which were determined experimentally from vertical-cavity surface emitting lasers with the same active region [56]. The gain and current density can be related by [54]

$$g_{th} = g_0 \ln \left( \frac{\eta_i J_{th}}{N_{QW} J_{tr}} \right) \quad (4)$$

where $g_{th}$, $J_{th}$, and $J_{tr}$ are threshold gain required to reach at threshold, threshold current density and transparency current density, respectively. Considering the threshold material gain $g_{th} = 1000$ cm$^{-1}$ and calculated longitudinal confinement factor $\Gamma_z = 7.6\%$, we calculate modal threshold gain 76 cm$^{-1}$. Table IV lists the parameters of an example design for an SG-DBR laser at 2.56 $\mu$m.

TABLE IV
2.6 $\mu$M SG-DBR DEVICE PARAMETER SPECIFICATION

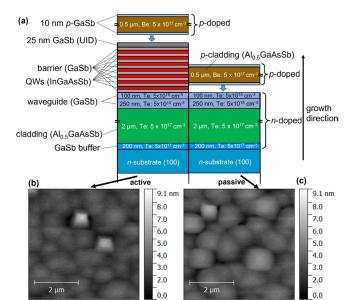| Property | Value | Unit |
|---|---|---|
| Modal threshold gain | 76 | cm$^{-1}$ |
| $g_o$ | 1400 | cm$^{-1}$ |
| transparency current density / well | 200 | A/cm$^2$ |
| Internal efficiency | 0.4 | % |
| Gain length | 700 | $\mu$m |
| Waveguide width | 5 | $\mu$m |
| # QWs | 7 | |
| Threshold current (calculated) | 130 | mA |



Fig. 7. (a) Schematic cross-sectional view of offset quantum-well epitaxial structure – active (left), passive (right) regions with the regrown epilayers on top. 5 $\mu$m × 5 $\mu$m AFM images of the (b) active (with MQWs) and (c) passive areas (etched MQWs) after MBE regrowth.

## G. Phase Tuner Design

The phase tuner section of GaSb-based tunable lasers exploit the carrier injection based free-carrier plasma effect. This changes refractive index that eventually changes the phase of incoming optical waves as well as makes a blueshift of resonant wavelengths. Under current injection with the injection efficiency $\eta_i = 0.6$ and tuning current $I_t = 5$ mA into the passive region provide a carrier density $N$ calculated by Eqn. (5).

$$N = \sqrt{\frac{\eta_i I_t}{q V_t B}} \qquad (5)$$

where $V_t$ denotes the volume of the tuning region, the bimolecular recombination constant of GaSb $B = 1.2 \times 10^{-10}$ cm$^3$/sec. Considering the passive waveguide region with 450 nm thickness, 4 $\mu$m width and 80 $\mu$m length, the carrier density is calculated to be $1.2 \times 10^{18}$ cm$^{-3}$. Taking $\lambda = 2560$ nm, speed of light in free-space $c = 3 \times 10^8$ m/sec $n_{GaSb} = 3.85$, the effective masses of electron $m_e = 0.041*m_0$, and holes $m_h = 0.4*m_0$, transverse confinement factor for the waveguide region $\Gamma_{wg} = 0.55$, the mobilities of electrons and holes $\mu_e = 3000$ cm$^2$/V-sec and $\mu_h = 1000$ cm$^2$/V-sec, $\varepsilon_0$ is the permittivity of free-space, ambipolar injection of $N = P = 1.2 \times 10^{18}$ cm$^{-3}$, an index change $\Delta n = -0.025$ and an optical loss $\alpha_{Pl} = 4.2$ cm$^{-1}$ are obtained

$$\Delta n = -\Gamma_{wg} \frac{q^2 \lambda^2}{8\pi^2 c^2 n \varepsilon_0} \left(\frac{1}{m_e^*} + \frac{1}{m_h^*}\right) N \qquad (6)$$

$$\alpha_{pl} = -\Gamma_{wg} \frac{q^3 \lambda^2}{4\pi^2 c^3 n \varepsilon_0} \left(\frac{1}{m_e^{*2}\mu_e} + \frac{1}{m_h^{*2}\mu_h}\right) N \qquad (7)$$

Hence, a passive waveguide section of length $L_p$ with an electronically controllable effective refractive index serves as the basic tuning element to perform the shift of the resonance wavelength. As the (single-pass) phase shift of this element $\Delta\Phi = 2\pi/\lambda * \Delta n * L_p$ is proportional to the product of effective refractive index and length, it is important for a strong tuning effect to extend this element over a major part of the laser cavity. Considering $L_p = 51$ $\mu$m, $\lambda = 2560$ nm and $\Delta n = -0.025$, a phase shift of $\pi$ radians can be achieved. In addition to the magnitude of the index change, optical absorption losses should also be considered in the design of phase tuners.

## H. Regrowth

To confirm the feasibility of the design of S-MWIR PICs, active/passive regions were defined on the MBE-grown base epitaxial structure shown in Fig. 7. Passive regions were formed by selectively removing the multiple-QW active region from the base structure. Low-temperature-based (450°C) *in situ* atomic hydrogen cleaning was employed for deoxidizing the growth surface after selectively removing the MQW region. The etch details can be found elsewhere [59]. Blanket MBE regrowth was then performed by the deposition of a thick quaternary cladding layer on Al-free surfaces. Figs. 7(b) and (c) show the AFM images of the surface morphology of both active and passive regions. Atomic steps were observed after MBE regrowth in both active and passive areas with and without MQWs, respectively. The film exhibits surface morphology with a root-mean-square (RMS) roughness value of <0.3 nm, as shown in Figs. 7(b)-(c). Although the surface morphology shows coalescing mound-like structures in our first attempt, a flatter, terraced surface is desired, which will be investigated in our future studies.

## V. CONCLUSION AND OUTLOOK

This study aims to transition this mature laser tuning technology to the S-MWIR by developing a GaSb PIC technology with InGaAsSb/AlGaAsSb/GaSb gain material. We have proposed GaSb-based widely-tunable laser diode which consists of an offset QW-based structure integrated with an SG-DBR monolithically. This paper focuses on developing a high-performance PIC technology for, in particular, around 2.6 $\mu$m wavelengths using type-I diode lasers, although many of the same advances will later be applicable to the 2.2-3.4 $\mu$m wavelength region using type-I and ICLs operating at 3-6 $\mu$m. The presented concepts and encouraging materials growth results pave the way for the realization of transmitter PICs covering a large SWIR wavelength range using GaSb-technology.

Beyond classical photonics, on-chip lasers in S-MWIR will also expand the range of quantum states of light generation

significantly. In an interaction-free imaging technique [60], a pair of entangled photons in telecom and MWIR are generated through nonlinear optical interactions. The MWIR photon of the pair interacts with samples while its partner telecom photon is detected by well-established and high efficiency single-photon detectors in telecom wavelength. Due to the phenomenon of entanglement, the non-interacted telecom photon provides information about the sample which interacted with the non-detected MWIR photon. An S-MWIR and tunable laser will allow generation of the pairs in higher MWIR wavelengths (limited by the material transparency), thus covering a wider sensing range [61]. The integration of this laser on-chip will allow phase stable, complex and portable version of such techniques.

## REFERENCES

[1] B. Pejcic, M. Myers, and A. Ross, "Mid-infrared sensing of organic pollutants in aqueous environments," *Sensors*, vol. 9, no. 8, pp. 6232–6253, Aug. 2009.

[2] I. E. Gordon et al., "The HITRAN2016 molecular spectroscopic database," *J. Quantum Spectrosc. Radiat. Transf.*, vol. 203, pp. 3–69, Dec. 2017.

[3] I. Kviatkovsky, H. M. Chrzanowski, E. G. Avery, H. Bartolomaeus, and S. Ramelow, "Microscopy with undetected photons in the mid-infrared," *Sci. Adv.*, vol. 6, no. 42, Oct. 2020, Art. no. eabd0264.

[4] C. Mitra, "Mid-infrared spectroscopy and challenges in industrial environment," in *Infrared Spectroscopy: Principles, Advances, and Applications*, M. El-Azazy, Ed. London, U.K.: IntechOpen, 2018.

[5] V. A. Serebryakov, É. V. Boĭko, N. N. Petrishchev, and A. V. Yan, "Medical applications of mid-IR lasers. Problems and prospects," *J. Opt. Technol.*, vol. 77, no. 1, pp. 6–17, Jan. 2010.

[6] F. Toor, S. Jackson, X. Shang, S. Arafin, and H. Yang, "Mid-infrared lasers for medical applications: Introduction to the feature issue," *Biomed. Opt. Exp.*, vol. 9, no. 12, pp. 6255–6257, Nov. 2018.

[7] P. L. Hanst and S. T. Hanst, *Gas Measurements in the Fundamental Infrared Region* (Chemistry Analytical Series). New York, NY, USA: Wiley, 1994, pp. 335–470.

[8] M. Ebrahim-Zadeh and K. Vodopyanov, "Mid-infrared coherent sources and applications: Introduction," *J. Opt. Soc. Amer. B, Opt. Phys.*, vol. 33, no. 11, p. MIC1, Nov. 2016.

[9] F. K. Tittel, D. Richter, and A. Fried, "Mid-Infrared laser applications in spectroscopy," in *Solid-State Mid-Infrared Laser Sources*, I. T. Sorokina and K. L. Vodopyanov, Eds. Berlin, Germany: Springer, 2003, pp. 458–529.

[10] J. Chen, A. Hangauer, R. Strzoda, and M.-C. Amann, "VCSEL-based calibration-free carbon monoxide sensor at 2.3 $\mu$m with in-line reference cell," *Appl. Phys. B, Lasers Opt.*, vol. 102, no. 2, pp. 381–389, Feb. 2011.

[11] N. S. Prasad, "Optical Communications in the mid-wave IR spectral band," in *Free-Space Laser Communications: Principles and Advances*. New York, NY, USA: Springer, 2008, pp. 347–391.

[12] J. R. Meyer, I. Vurgaftman, R. Q. Yang, and L. R. Ram-Mohan, "Type-II and type-I interband cascade lasers," *Electron. Lett.*, vol. 32, no. 1, pp. 45–46, 1996.

[13] N. Hattasan, B. Kuyken, F. Leo, E. M. P. Ryckeboer, D. Vermeulen, and G. Roelkens, "High-efficiency SOI fiber-to-chip grating couplers and low-loss waveguides for the short-wave infrared," *IEEE Photon. Technol. Lett.*, vol. 24, no. 17, pp. 1536–1538, Sep. 2012.

[14] E. Ryckeboer et al., "Silicon-on-insulator spectrometers with integrated GaInAsSb photodiodes for wide-band spectroscopy from 1510 to 2300 nm," *Opt. Exp.*, vol. 21, no. 5, pp. 6101–6108, 2013.

[15] K. Vizbaras and M.-C. Amann, "Room-temperature 3.73 $\mu$m GaSb-based type-I quantum-well lasers with quinternary barriers," *Semicond. Sci. Technol.*, vol. 27, no. 3, Jan. 2012, Art. no. 032001.

[16] S. D. Sifferman et al., "Highly strained mid-infrared type-I diode lasers on GaSb," *IEEE J. Sel. Topics Quantum Electron.*, vol. 21, no. 6, pp. 1–10, Nov. 2015.

[17] G. Belenky, L. Shterengas, G. Kipshidze, and T. Hosoda, "Type-I diode lasers for spectral region above 3 $\mu$m," *IEEE J. Sel. Topics Quantum Electron.*, vol. 17, no. 5, pp. 1426–1434, Oct. 2011.

[18] R. Q. Yang, "Infrared laser based on intersubband transitions in quantum wells," *Superlattices Microstruct.*, vol. 17, no. 1, pp. 77–83, Jan. 1995.

[19] I. Vurgaftman et al., "Rebalancing of internally generated carriers for mid-infrared interband cascade lasers with very low power consumption," *Nature Commun.*, vol. 2, no. 1, p. 585, 2011.

[20] I. Vurgaftman et al., "Interband cascade lasers," *J. Phys. D, Appl. Phys.*, vol. 48, no. 12, p. 123001, Mar. 2015.

[21] R. Q. Yang et al., "InAs-based interband cascade lasers," *IEEE J. Sel. Topics Quantum Electron.*, vol. 25, no. 6, pp. 1–8, Nov./Dec. 2019.

[22] J. R. M. Faist, *Quantum Cascade Lasers*. Oxford, U.K.: Oxford Univ. Press, 2013.

[23] R. M. Jerry, V. Igor, and W. Gerard, "Special section guest editorial: Quantum and interband cascade lasers with applications," *Opt. Eng.*, vol. 57, no. 1, pp. 1–2, 2018.

[24] I. Vurgaftman et al., "Interband cascade lasers," in *Proc. Conf. Lasers Electro-Opt.* Virtual: Optica Publishing Group, 2020, Paper STh1E.6.

[25] Y. Gu et al., "2.4 $\mu$m InP-based antimony-free triangular quantum well lasers in continuous-wave operation above room temperature," *Appl. Phys. Exp.*, vol. 7, no. 3, Mar. 2014, Art. no. 032701.

[26] G. Boehm et al., "Growth of InAs-containing quantum wells for InP-based VCSELs emitting at 2.3 $\mu$m," *J. Cryst. Growth*, vols. 301–302, pp. 941–944, Apr. 2007.

[27] L. A. Coldren, "Monolithic tunable diode lasers," *IEEE J. Sel. Top. Quantum Electron.*, vol. 6, no. 6, pp. 988–999, Dec. 2000.

[28] S. Matsuo and T. Segawa, "Microring-resonator-based widely tunable lasers," *IEEE J. Sel. Topics Quantum Electron.*, vol. 15, no. 3, pp. 545–554, May/Jun. 2009.

[29] J. R. Meyer et al., "Interband cascade photonic integrated circuits on native III–V chip," *Sensors*, vol. 21, no. 2, p. 599, 2021.

[30] M. Sieger and B. Mizaikoff, "Toward on-chip mid-infrared sensors," *Anal. Chem.*, vol. 88, no. 11, pp. 5562–5573, Jun. 2016.

[31] S. A. Miller et al., "Low-loss silicon platform for broadband mid-infrared photonics," *Optica*, vol. 4, no. 7, p. 707, 2017.

[32] M. Muneeb et al., "Demonstration of silicon-on-insulator mid-infrared spectrometers operating at 3.8 $\mu$m," *Opt. Exp.*, vol. 21, no. 10, pp. 11659–11669, May 2013.

[33] G. Sun, R. A. Soref, and H. H. Cheng, "Design of a Si-based lattice-matched room-temperature GeSn/GeSiSn multi-quantum-well mid-infrared laser diode," *Opt. Exp.*, vol. 18, no. 19, pp. 19957–19965, 2010.

[34] R. Wang, A. Malik, I. Šimonytė, A. Vizbaras, K. Vizbaras, and G. Roelkens, "Compact GaSb/silicon-on-insulator 2.0× $\mu$m widely tunable external cavity lasers," *Opt. Exp.*, vol. 24, no. 25, pp. 28977–28986, Dec. 2016.

[35] R. Wang et al., "Widely tunable 2.3 $\mu$m III–V-on-silicon Vernier lasers for broadband spectroscopic sensing," *Photon. Res.*, vol. 6, no. 9, p. 858, 2018.

[36] R. Wang et al., "III–V-on-silicon photonic integrated circuits for spectroscopic sensing in the 2–4 $\mu$m wavelength range," *Sensors*, vol. 17, no. 8, p. 1788, 2017.

[37] A. Spott et al., "Heterogeneously integrated interband cascade lasers on silicon," in *Proc. IEEE Int. Semiconductor Laser Conf. (ISLC)*, Sep. 2018, pp. 1–2.

[38] A. Spott et al., "Interband cascade laser on silicon," *Optica*, vol. 5, no. 8, pp. 996–1005, Aug. 2018.

[39] A. Spott, E. J. Stanton, N. Volet, J. D. Peters, J. R. Meyer, and J. E. Bowers, "Heterogeneous integration for mid-infrared silicon photonics," *IEEE J. Sel. Topics Quantum Electron.*, vol. 23, no. 6, pp. 1–10, Nov. 2017.

[40] I. Vurgaftman et al., "Ultra-broadband photonic integrated circuit platform and ultra-broadband photonic integrated circuit," U.S. Patent 2016/0 109 655 A1, Apr. 21, 2016.

[41] S.-P. Ojanen et al., "GaSb diode lasers tunable around 2.6 $\mu$m using silicon photonics resonators or external diffractive gratings," *Appl. Phys. Lett.*, vol. 116, no. 8, Feb. 2020, Art. no. 081105.

[42] J. W. Raring and L. A. Coldren, "40-Gb/s widely tunable transceivers," *IEEE J. Sel. Top. Quantum Electron.*, vol. 13, no. 1, pp. 3–14, 2007.

[43] M. N. Sysak, L. A. Johansson, J. W. Raring, M. Rodwell, L. A. Coldren, and J. Bowers, "A high efficiency, current injection based quantum-well phase modulator monolithically integrated with a tunable laser for coherent systems," in *Proc. Conf. COTA*. Whistler, BC, Canada: Optica Publishing Group, 2006, Paper CFC6.

[44] E. Skogen, *Quantum Well Intermixing for Wavelength-Agile Photonic Integrated Circuits*. Santa Barbara, CA, USA: Univ. of California Santa Barbara, Department of Electrical and Computer Engineering, 2003.

[45] A. W. Fang, H. Park, O. Cohen, R. Jones, M. J. Paniccia, and J. E. Bowers, "Electrically pumped hybrid AlGaInAs-silicon evanescent laser," *Opt. Exp.*, vol. 14, no. 20, pp. 9203–9210, 2006.

[46] C. Merritt et al., "Effects of ion bombardment on interband cascade laser structures," *Proc. SPIE*, vol. 11288, Jan. 2020, Art. no. 112881N.

[47] A. Dehzangi, D. Wu, R. McClintock, J. Li, and M. Razeghi, "Planar nBn type-II superlattice mid-wavelength infrared photodetectors using zinc ion-implantation," *Appl. Phys. Lett.*, vol. 116, no. 22, Jun. 2020, Art. no. 221103.

[48] M. Lu, *Integrated Optical Phase-Locked Loops*. Santa Barbara, CA, USA: Univ. of California Santa Barbara, Department of Electrical and Computer Engineering, 2013.

[49] S. Arafin and L. A. Coldren, "Advanced InP photonic integrated circuits for communication and sensing," *IEEE J. Sel. Topics Quantum Electron.*, vol. 24, no. 1, pp. 1–12, Jan./Feb. 2018.

[50] *Ansys Lumerical MODE*. Accessed: Jan. 14, 2023. [Online]. Available: https://www.ansys.com/products/photonics/mode

[51] A. Salhi et al., "Single-frequency Sb-based distributed-feedback lasers emitting at 2.3 $\mu$m above room temperature for application in tunable diode laser absorption spectroscopy," *Appl. Opt.*, vol. 45, no. 20, pp. 4957–4965, 2006.

[52] J. A. Gupta, P. J. Barrios, J. Lapointe, G. C. Aers, C. Storey, and P. Waldron, "Modal gain of 2.4 $\mu$m InGaAsSb–AlGaAsSb complex-coupled distributed-feedback lasers," *IEEE Photon. Technol. Lett.*, vol. 21, no. 20, pp. 1532–1534, Oct. 2009.

[53] L. Shterengas, G. L. Belenky, J. G. Kim, and R. U. Martinelli, "Design of high-power room-temperature continuous-wave GaSb-based type-I quantum-well lasers with $\lambda > 2.5$ $\mu$m," *Semicond. Sci. Technol.*, vol. 19, no. 5, p. 655, 2004.

[54] L. A. Coldren, S. W. Corzine, and M. L. Mashanovitch, *Diode Lasers and Photonic Integrated Circuits*. Hoboken, NJ, USA: Wiley, 2012.

[55] S. Arafin, A. Bachmann, and M. Amann, "Transverse-mode characteristics of GaSb-based VCSELs with buried-tunnel junctions," *IEEE J. Sel. Topics Quantum Electron.*, vol. 17, no. 6, pp. 1576–1583, Nov. 2011.

[56] S. Arafin, "Electrically-pumped GaSb-based vertical-cavity surface-emitting lasers," Ph.D. dissertation, Dept. Elect. Eng., Tech. Univ. Munich, Munich, Germany, 2012.

[57] K. Kashani-Shirazi, K. Vizbaras, A. Bachmann, S. Arafin, and M.-C. Amann, "Low-threshold strained quantum-well GaSb-based lasers emitting in the 2.5- to 2.7-$\mu$m wavelength range," *IEEE Photon. Technol. Lett.*, vol. 21, no. 16, pp. 1106–1108, Aug. 2009.

[58] K. Vizbaras et al., "MBE growth of low threshold GaSb-based lasers with emission wavelengths in the range of 2.5–2.7 $\mu$m," *J. Cryst. Growth*, vol. 323, no. 1, pp. 446–449, May 2011.

[59] S. Arafin et al., "Study of wet and dry etching processes for antimonide-based photonic ICs," *Opt. Mater. Exp.*, vol. 9, no. 4, pp. 1786–1794, Apr. 2019.

[60] G. B. Lemos, V. Borish, G. D. Cole, S. Ramelow, R. Lapkiewicz, and A. Zeilinger, "Quantum imaging with undetected photons," *Nature*, vol. 512, no. 7515, pp. 409–412, Aug. 2014.

[61] R. A. McCracken, F. Graffitti, and A. Fedrizzi, "Numerical investigation of mid-infrared single-photon generation," *J. Opt. Soc. Amer. B, Opt. Phys.*, vol. 35, no. 12, pp. C38–C48, Dec. 2018.

**Weicheng You** was born in Sichuan, China. He received the B.S. degree in electronics engineering from Sichuan University, Sichuan, in 2017, and the M.S. degree in electrical engineering from The Ohio State University, Columbus, OH, USA, in 2019, where he is currently pursuing the Ph.D. degree.

**Sarvagya Dwivedi** (Member, IEEE) received the master's degree in electrical engineering from IIT Bombay and the Ph.D. degree in photonics engineering from Photonics Research Group, Ghent University-Imec, Belgium. He then worked as a Post-Doctoral Research Associate at the University of California Santa Barbara, Santa Barbara, CA, USA. He has more than nine years of experience in the areas of all-silicon, silicon nitride, and Ge-on-Si based tolerant devices and circuits for various applications, like datacom, telecom, and mid-infrared sensing. Currently, he is a Senior Staff Engineer and photonics integration circuit (PIC) lead with Rockley Photonics, Pasadena, CA, USA. He has authored and coauthored over 50 publications.

**Imad I. Faruque** received the B.Sc. degree in electrical and electronic engineering from the Bangladesh University of Engineering and Technology in 2009, the joint Erasmus Mundus M.S. degree in photonics from Universiteit Gent, Vrije Universiteit Brussel, University of St Andrews, and Heriot-Watt University in 2012, and the Ph.D. degree from the Quantum Engineering Technology Laboratory (QET Labs), University of Bristol, U.K., in 2018. During his Ph.D., he worked on heralded single-photon sources in silicon photonics, and afterwards as a Post-Doctoral Researcher, he worked on various quantum communication and quantum metrology projects. Currently, he is a Senior Post-Doctoral Research Associate with the University of Bristol.

**Demis D. John** received the B.S. degree from the University of Massachusetts, Lowell, MA, USA, in 2005, and the M.S. and Ph.D. degrees in electrical engineering from the University of California, Santa Barbara, CA, USA, in 2007 and 2012, respectively, focusing on the development of ultralow-loss optical waveguides for photonic integrated circuits. He currently works with the Nanofabrication Facility, a research cleanroom, University of California, Santa Barbara. His expertise is fabrication and process development for nanotechnology devices, especially photonic devices.

**Anthony P. McFadden** received the B.S. degree in electrical engineering and applied math from UNM, Albuquerque, New Mexico, and the Ph.D. degree in electrical engineering from Palmstrom Group in Summer 2017. He joined UCSB, in Fall 2010. He was a Post-Doctoral Researcher until Summer 2020. As a Post-Doctoral Researcher, he worked on developing widely tunable III-AsSb based lasers in the 2.2–2.6 $\mu$m range. He also studied different growth techniques for superconductor-semiconductor-superconductor trilayers for superconducting qubits. In Summer 2020, he moved to Boulder, CO with his family to work as a Staff Scientist at NIST. He remains a collaborator with the group as a Visiting Scientist.

**Christopher J. Palmstrøm** (Fellow, IEEE) received the B.S. degree in physics and electronic engineering and the Ph.D. degree in electrical and electronic engineering from the University of Leeds, Leeds, U.K., in 1975 and 1979, respectively. From 1980 to 1985, he was a Post-Doctoral Research Associate and a Research Associate at the Department of Materials Science and Engineering, Cornell University, Ithaca, NY, USA, doing research on semiconductor materials, contact technologies, ion beam analysis, and polymer/polymer interdiffusion. Since 2007, he has been a Faculty Member with the Department of Electrical and Computer Engineering and the Department of Materials, University of California at Santa Barbara, Santa Barbara. His current research interests include combining in situ surface science characterization with molecular beam epitaxial growth of electronic, photonic, thermoelectric, magnetic, spintronic, shape memory, and multifunctional oxide heterostructure materials.

**Larry A. Coldren** (Life Fellow, IEEE) received the Ph.D. degree in electrical engineering from Stanford University, Stanford, CA, in 1972. After 13 years in the research area with Bell Laboratories, he joined the University of California at Santa Barbara (UCSB) in 1984. From 2009 to 2011, he served as the Dean of the College of Engineering. At UCSB, he has worked on multiple-section widely-tunable lasers and efficient vertical-cavity surface-emitting lasers (VCSELs). More recently, his group has developed high-performance InP-based photonic integrated circuits and high-speed VCSELs. He is currently the Fred Kavli Professor of optoelectronics and sensors and holds appointments with the Department of Materials and the Department of Electrical and Computer Engineering, UCSB. He has authored or coauthored over 1000 journal and conference papers, coauthored eight book chapters, a widely used textbook, and holds 65 patents. He is a fellow of OSA and IEE and a member of the National Academy of Engineering. He was a recipient of the 2004 John Tyndall Award, the 2009 Aron Kressel Award, the 2014 David Sarnoff Award, and the 2015 IPRM Award.

**Shamsul Arafin** (Senior Member, IEEE) is working as an Assistant Professor with the Electrical and Computer Engineering Department, The Ohio State University. He has more than 13 years of experiences on the design, fabrication of widely tunable semiconductor lasers, including vertical-cavity surface emitting lasers (VCSELs). Till now, he has authored or coauthored over 120 publications in the areas of III–V materials, the corresponding devices, and InP-based photonic integrated circuits and has given numerous invited and contributed talks at various international conferences. He is a Senior Member of OSA and SPIE.